METALLURGY

Superior resistance to cyclic creep in a gradient structured steel

Qingsong Pan[1]†, Kunqing Ding[2]†, Song Guo[1,3]†, Ning Lu[4], Nairong Tao[1], Ting Zhu[2]*, Lei Lu[1]*

Cyclic creep, or ratcheting, is a severe form of fatigue deformation caused by cumulative unidirectional plastic strain under asymmetrical stress cycling with a nonzero mean stress. It often causes premature failure of structural materials, and enhancing ratcheting resistance is a challenge in materials engineering. We demonstrate superior ratcheting resistance in high-strength austenitic stainless steel with a gradient hierarchy of dislocation cells. The ratcheting rate is two to four orders of magnitude lower than for coarse-grained counterparts. Its resistance results from sustained microstructural refinement through deformation-induced coherent martensitic transformations to hexagonal close-packed nanolayers within stable dislocation cells. The progressively refined microstructure mitigates cyclic softening and suppresses strain localization during stress cycling, thus reducing ratcheting strain. The gradient dislocation architecture represents a promising design for high-strength, ratcheting-resistant materials.

Service failures in structural components such as turbine blades, pressure vessels, nuclear pipes, and offshore structures can lead to substantial financial costs and even loss of life (*1*–*3*). When metallic materials are subjected to asymmetrical stress cycling with nonzero mean stresses, a continuously increasing unidirectional strain commonly takes place, a phenomenon known as cyclic creep, or ratcheting (*2*–*8*). Ratcheting accelerates due to cyclic softening and strain localization, particularly when the applied stress exceeds the material's yield strength under prolonged conditions (*9*–*13*).

Various material design strategies, whether through tuning chemical composition, microstructure, or both, struggle to balance strengthening with ratcheting resistance (*1*–*3*, *9*, *11*). The ratcheting response worsens as the strength increases in most conventional single-principal-element alloys (*3*, *9*, *14*, *15*) and multi-principal-element alloys (*16*). For example, prestraining typically increases strength and improves short-term ratcheting resistance in materials with coarse grains (CGs) during early stress cycles (*17*). However, it reduces hardening capacity and promotes strain localization, weakening long-term ratcheting resistance (*3*, *9*). Nanostructured and heavily deformed materials, with abundant high-angle grain boundaries (GBs) and dense dislocations, also fail to achieve this balance. Although these materials resist ratcheting initially, they soften and coarsen under repeated cycles due to limited work hardenability and severe strain localization. These effects accelerate ratcheting, leading to early cracking and failure under prolonged asymmetrical stress cycling (*11*, *18*–*21*). A similar trend of weakened ratcheting resistance has been observed in high-strength dual-phase steels, primarily attributed to cyclic softening resulting from limited strain hardening and rapid dynamic recovery (*3*, *22*).

To improve the ratcheting resistance of high-strength materials, it is essential to mitigate cyclic softening and suppress strain localization under asymmetrical cyclic loading. Achieving this requires tailoring the microstructure to enhance strain-hardening capability, minimize dynamic recovery to mitigate cyclic softening, and prevent structural coarsening to control strain localization during asymmetrical cycling. Recently, a single-phase multi-principal-element alloy exhibited strong strengthening and hardening performance under monotonic tensile deformation, resulting in exceptional strength and ductility (*23*, *24*). This alloy features a hierarchical microstructure composed of stable, sample-level, gradient dislocation structure (GDS) confined within CGs. Therefore, exploiting the gradient dislocation architecture to enhance ratcheting resistance under asymmetrical cyclic stresses is of interest. In this study, we choose cost-effective austenitic 304 stainless steel (SS), which is widely used in diverse safety-critical applications (*25*). However, like most single-phase CG metals and alloys, conventional 304 SS not only has a low yield strength but also suffers from limited ratcheting resistance (*2*).

GDS steel

We produced a GDS material using a single-phase face-centered cubic (FCC) AISI 304 SS (Fe–18%Cr–8%Ni by weight percent). The initial sample consisted of randomly oriented, equiaxed CGs with an average size of ~37 μm (fig. S1, A to C). Dog-bone–shaped bar specimens with a gauge diameter of 6 mm and a gauge length of 13 mm were processed through cyclic torsion at ambient temperature (fig. S1D). After this treatment, equiaxed CGs from the surface to the core of the sample were homogeneously distributed, similar to those before cyclic torsion, as indicated by electron backscatter diffraction (EBSD) with scanning electron microscopy (SEM) (Fig. 1A). A prominent feature of GDS SS is the profuse dislocation cells with low-angle boundaries having misorientations of <15° distributed in most grains in the topmost layer (within ~100 μm from the surface) (Fig. 1, B to E). The low-angle boundary density (or cell size) gradually decreases (or increases) with depth from the top surface (Fig. 1B) due to the applied torsion, which generates radially gradient plastic strains in the sample cross section (fig. S1, E to G). At the core, the prevailing dislocation patterns in grains are individual planar dislocations and loose tangles (fig. S1, I and J). Thus, a sample-level GDS microstructure extending from the surface to the core was achieved in 304 SS after cyclic torsion. This GDS 304 SS retains a single-phase FCC structure, as confirmed by EBSD and transmission electron microscopy (TEM) (Fig. 1).

SEM and TEM observations revealed that the abundant equiaxed dislocation cells in the topmost grains are ~290 nm in size (Fig. 1, C to E). The cell walls, ~50 nm thick, contain a high density of dislocations (0.8×10^{15} m^{-2}) and exhibit small misorientations of ~0.6°, as estimated by orientation mapping (Fig. 1E). By contrast, the cell interiors contain fewer dislocations (Fig. 1F). The surface of GDS SS exhibits relatively low residual stress, ~70 MPa (fig. S1H), attributed to the nearly pure shear plastic strain imposed without any surface tooling. This contrasts with conventional processing methods such as shot peening (*26*). The GDS sample showed a pronounced gradient distribution of microhardness ranging from 2.0 GPa in the central region to 3.2 GPa at the topmost surface, which is higher than ~1.9 GPa of dislocation-free CGs (fig. S2).

Ratcheting resistance under asymmetrical stress cycling

We characterized both the uniaxial tensile and cyclic ratcheting performance of GDS SS at ambient temperature. Quasistatic uniaxial tensile tests showed an elevated yield strength (σ_y at 0.2% offset) of 489 ± 2 MPa, ~130% higher than that of CG counterparts (210 ± 5 MPa) (fig. S3A). A high uniform elongation (ε_u) of up to 52 ± 1% was measured for GDS SS, lower than that of CG counterparts (71 ± 1%). This combination of yield strength and uniform elongation in GDS 304 SS surpasses that of high-performance SS strengthened by nanotwin

[1]Shenyang National Laboratory for Materials Science, Institute of Metal Research, Chinese Academy of Sciences, Shenyang, P.R. China. [2]Woodruff School of Mechanical Engineering, Georgia Institute of Technology, Atlanta, GA, USA. [3]School of Materials Science and Engineering, University of Science and Technology of China, Shenyang, P.R. China. [4]School of Chemistry and Chemical Engineering, Shandong University, Jinan, P.R. China.
*Corresponding author. Email: llu@imr.ac.cn (L.L.); ting.zhu@me.gatech.edu (T.Z.)
†These authors contributed equally to this work.

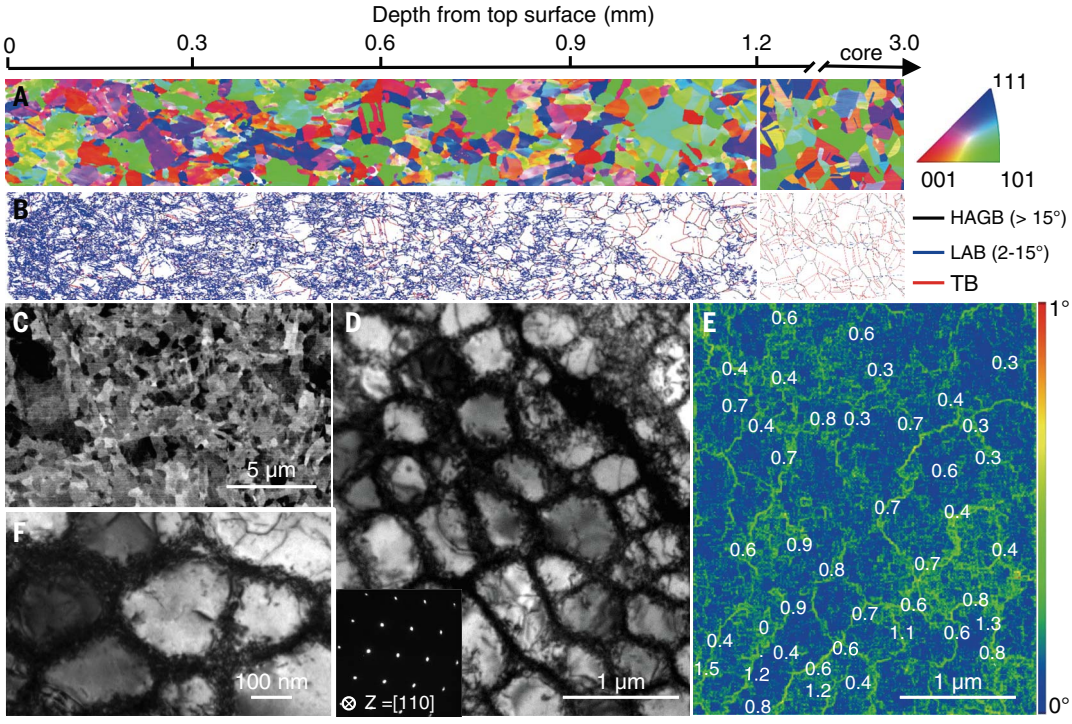

Fig. 1. Typical microstructure with gradient dislocation cells. (**A** and **B**) Cross-sectional EBSD images of GDS 304 SS processed by cyclic torsion showing the distributions of grain morphology and orientations (A) and internal boundaries [i.e., high-angle GBs (HAGBs), low-angle GBs (LABs), and TBs] with different misorientations (B) within an ~1.2 mm depth from the surface compared with those in the core. (**C** and **D**) Corresponding SEM and bright-field TEM images revealing dislocation cell structures at the topmost surface of the treated samples. The lower left inset in (D) shows the corresponding SAED patterns. (**E**) Misorientation angle of each cell wall measured using an electron precession diffraction technique in TEM. (**F**) Closer view of typical dislocation cells.

bundles and is comparable to additively manufactured hierarchical 316 SS (fig. S3B) (*27*).

We measured the ratcheting response of GDS 304 SS through asymmetrical tension-tension cyclic loading (stress control). Various combinations of maximum stress (σ_{max}) and minimum stress (σ_{min}) were applied while maintaining a stress ratio ($\sigma_{min}/\sigma_{max}$) of 0.1 and a frequency of 5 Hz (see table S1 for detailed loading parameters). Figure 2A shows a typical cyclic stress-strain curve of GDS SS tested at a σ_{max} of 510 MPa, which exhibits a substantially reduced progressive shift of the hysteresis loop along the tensile strain axis compared with CG SS (Fig. 2B). The GDS sample endured 10 million cycles without failure (~556 hours), reaching a cumulative ratcheting strain of ~2.1%. By contrast, the CG sample had a ratcheting-to-failure life (N_f) of 1.0×10^5 cycles (~5.6 hours) with a cumulative ratcheting strain of ~25.9%. The reduced cumulative ratcheting strain in the GDS sample results from its narrower hysteresis loop cycle by cycle (Fig. 2C), producing a much smaller ratcheting strain per cycle $\Delta\varepsilon_r$ than the CG counterpart at the same cycle number (Fig. 2D).

Improved ratcheting performance was also observed in bulk GDS 304 SS subjected to various σ_{max} ranging from 480 to 570 MPa (table S1). As shown in Fig. 2E, the cumulative ratcheting strain of GDS SS increased more slowly with increasing σ_{max} while exhibiting a longer ratcheting-to-failure life compared with the CG counterpart under the same σ_{max}. The cumulative ratcheting strain (8.7%) of the GDS sample cycled to failure at a σ_{max} of 570 MPa was smaller than that of the CG sample (~42%) at a lower σ_{max} of 420 MPa. By removing the inner core containing few dislocation cells, we obtained GDS tubular specimens (~0.75 mm thick), hereafter referred to as surface GDS. When tested at a high σ_{max} of 570 MPa, the surface GDS exhibited a lower cumulative ratcheting strain of 0.7% at a longer ratcheting life of 3.5×10^6 to 1.0×10^7 cycles (without failure) than the bulk GDS (fig. S3C). The instantaneous ratcheting rate of the surface GDS sample at a σ_{max} of 570 MPa was the smallest throughout the entire deformation stage compared with both CG and bulk GDS counterparts (fig. S3D). Using the equation $(\varepsilon_{max} - \varepsilon_{min})/2 - (\sigma_{max} - \sigma_{min})/2E$, where E is Young's modulus, the estimated plastic strain amplitude of surface GDS samples was found to gradually decrease under asymmetrical tension-tension cyclic loading but increased with higher σ_{max}, remaining smaller than that of bulk GDS and the CG counterpart under the same σ_{max} (fig. S3E).

We conducted additional cyclic experiments on bulk GDS samples under asymmetrical axial tension-compression and proportional axial-torsion stress-controlled cycling (multiaxial conditions; table S1). Figure S4, A and B, shows that GDS SS samples exhibit enhanced ratcheting resistance, with ratcheting strain rates two to three orders of magnitude lower than CG counterparts under negative stress ratios of −0.1 and −0.3. Similarly, exceptional ratcheting resistance was observed under combined axial and torsional fatigue conditions (fig. S4C), consistent with the results shown in Fig. 2. These findings confirm that the superior ratcheting resistance of GDS samples is an inherent property regardless of the stress ratio (positive or negative) or multiaxial mechanical loading.

Figure 2F presents the combinations of average ratcheting rate and maximum stress for a variety of metallic materials with different compositions and structures. The average ratcheting rate is defined as the cumulative ratcheting strain at failure, normalized by the fatigue life (cycles to failure), and the maximum stress is normalized by Young's modulus of the corresponding material. For the metals and alloys compared in Fig. 2F, the average ratcheting strain rate ranges from 10^{-6} to 10^{-3} and increases with applied maximum stress. By contrast, bulk GDS and surface GDS 304 SS exhibit average ratcheting strain rates as low as 10^{-10} to 10^{-6}, which are two to four orders of magnitude lower than those of their CG counterparts and high-strength steels with comparable strength (*2*, *3*, *20*, *22*). The low ratcheting rates of bulk GDS and surface GDS under high maximum stresses contrast with the accelerated ratcheting response in conventional transformation-induced plasticity (TRIP) steels (*15*), dual-phase steel (*3*), high-strength low alloy steel (*28*), additively manufactured SS (*20*), and deformed and nanostructured metallic materials (*3*, *18*, *19*, *21*).

Dynamic, coherently nanolayered martensitic transformation mechanism

To elucidate the underlying mechanisms responsible for the superior ratcheting resistance of GDS SS, we examined the deformation

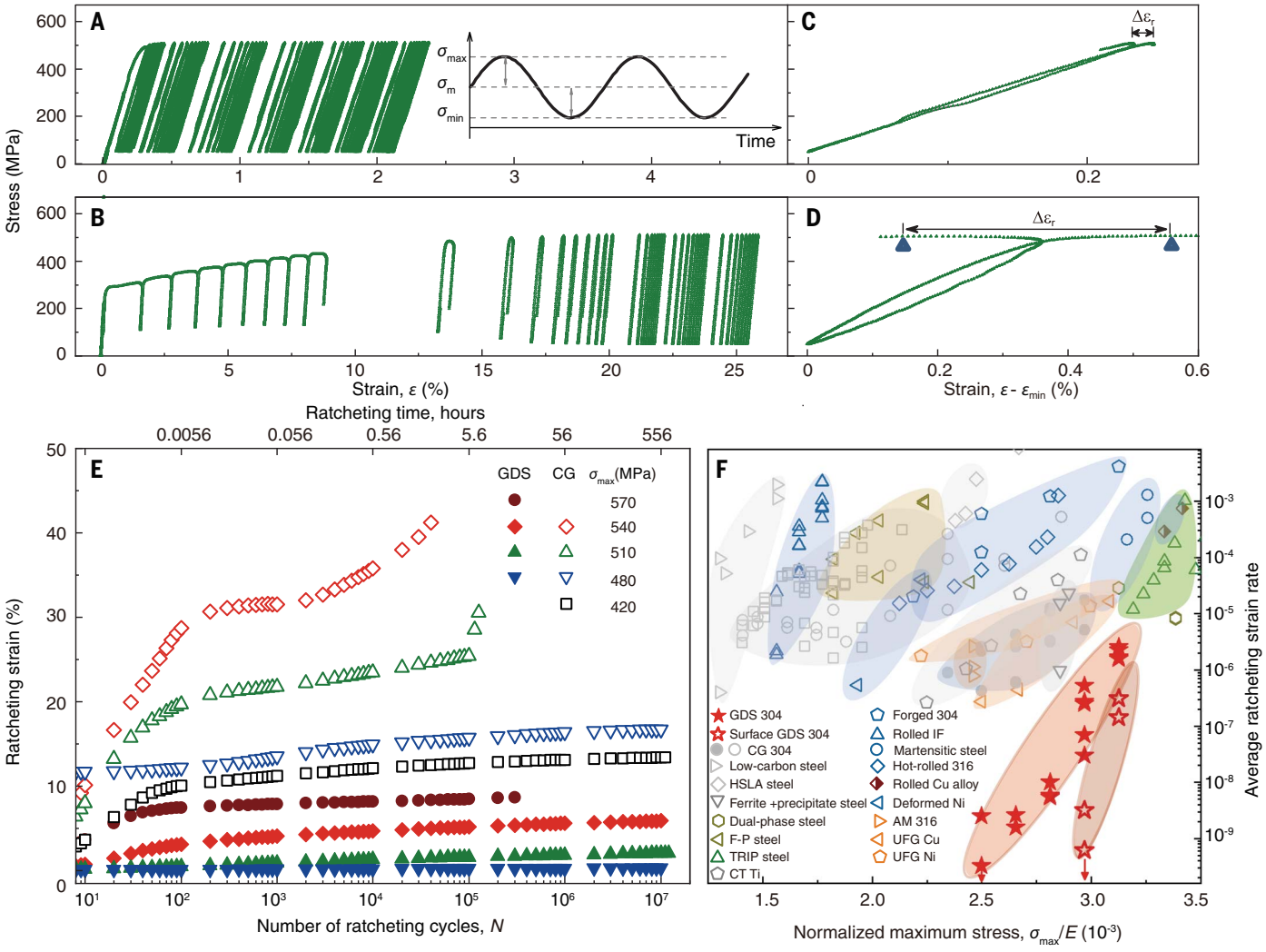

Fig. 2. Ratcheting response of GDS 304 SS at different maximum stresses. (**A** and **B**) Typical cyclic stress-strain evolution of GDS (A) and CG (B) samples subjected to asymmetrical tension-tension fatigue loading with a constant cyclic stress ratio ($\sigma_{min}/\sigma_{max}$) of 0.1 at a σ_{max} of 510 MPa. The upper right inset in (A) shows the sinusoidal loading curve under stress control. (**C** and **D**) Representative hysteresis loops for GDS (C) and CG (D) samples, with the origin of the strain axis in (C) and (D) shifted to allow comparison between the hysteresis loop. The ratcheting strain per cycle $\Delta\varepsilon_r$ is indicated by a double-headed arrow between two consecutive σ_{max} values in an individual hysteresis loop. (**E**) Ratcheting strain measured as a function of the number of cycles N for GDS and CG samples at various σ_{max} values. (**F**) Combinations of the average ratcheting strain rate and σ_{max} normalized by Young's modulus E for bulk and surface GDS samples compared with SS having homogeneous and heterogeneous microstructures (*3*, *14*), as well as representative structural materials, including martensitic steel (*2*), low-carbon steel (*3*), ferrite-pearlite (F-P) steel (*3*), TRIP steel (*15*), precipitate-strengthened steel (*22*), dual-phase steels (*3*), high-strength low-alloy (HSLA) steel (*28*), additively manufactured SS (*20*), and deformed and ultrafine-grained metals and alloys (*2*, *3*, *18*, *19*, *21*).

microstructure through interrupted testing of GDS samples cycled at a σ_{max} of 570 MPa. During the early stage of stress cycling (10% N_f), no significant structural changes were observed in the grains and dislocation cells (Fig. 3, A and B). However, numerous long, parallel microscale deformation bands with an average thickness of ~180 nm and spacing of ~3.5 μm began to form, with each band penetrating multiple cell walls in the topmost grains. The density of these bands decreased with depth from the top surface. Aberration-corrected high-angle annular dark-field scanning transmission electron microscopy (HAADF-STEM) revealed that these microscale deformation bands primarily consist of short stacking faults (SFs) (Fig. 3B), with an average length of ~25 nm and spacing of ~5.2 nm. As stress cycling progressed to 90% N_f, long, parallel microscale deformation bands continued to proliferate, resulting in an increased average thickness of ~320 nm and a decreased average band spacing of ~0.7 μm in the topmost grains (Fig. 3, C and D). Compared with the as-prepared GDS sample (Fig. 1), the size of the dislocation cells decreased slightly to ~217 nm, whereas the misorientation of the cell walls increased to ~1.1° (Fig. 3, D and E), accompanied by a higher density of dislocations (~1.3 × 10^{15} m^{-2}) at these cell walls.

The microscale deformation bands in GDS samples at 90% N_f were further characterized by selected area electron diffraction (SAED), bright-field TEM, and phase mapping (Fig. 3, D and E). These bands comprised newly formed hexagonal close-packed (HCP) nanolayers embedded in the FCC matrix, resulting in an HCP-FCC nanolaminate structure within each band. Atomic-resolution HAADF-STEM confirmed that each micrometer-long deformation band consisted of numerous multiple thin yet long HCP nanolayers, along with plenty of SFs and limited twin boundary (TB) segments within the FCC matrix (Fig. 3, F and G). The average length of the HCP nanolayers was ~160 nm,

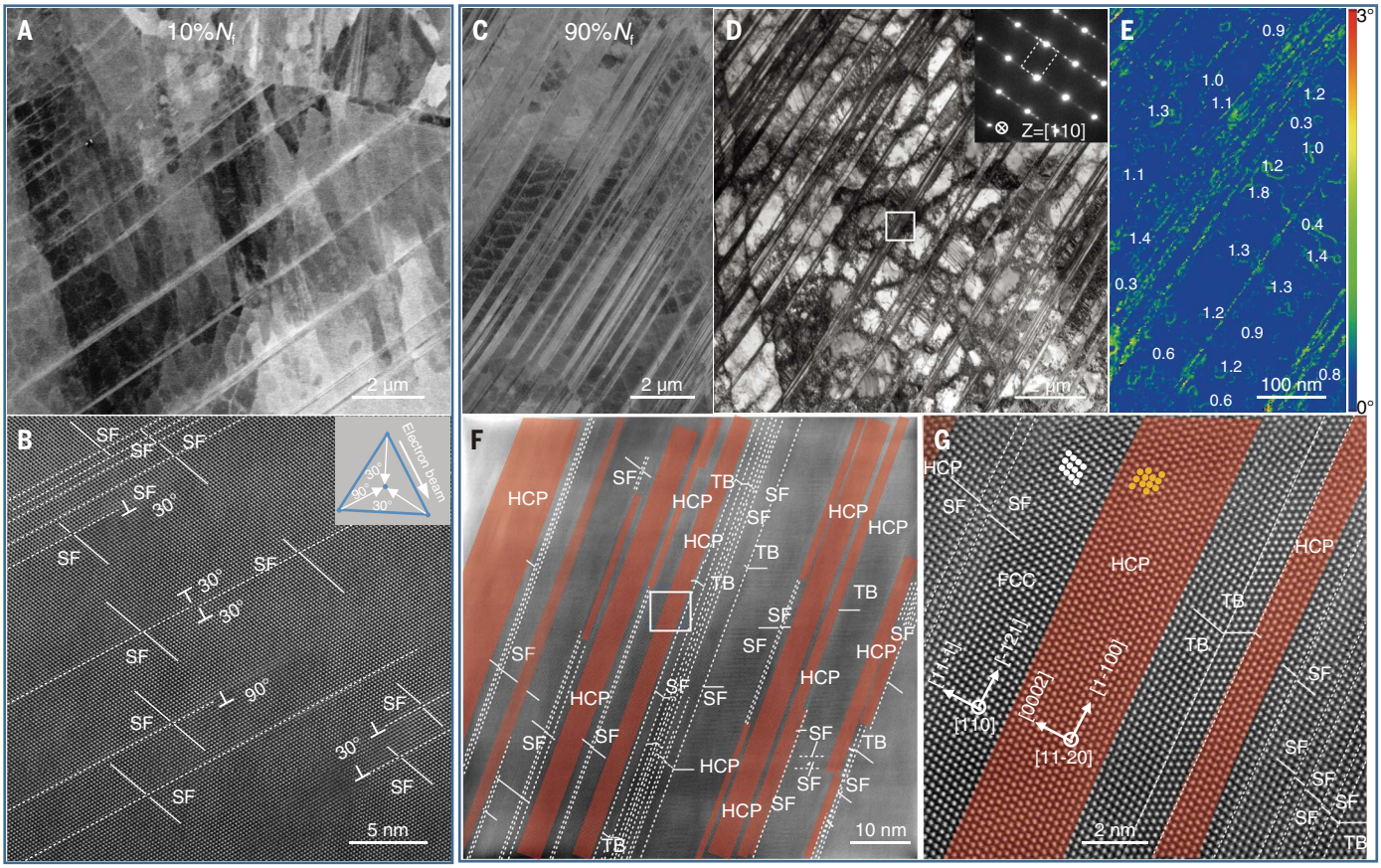

Fig. 3. Deformation microstructures of GDS 304 SS cycled under a σ_{max} of 570 MPa at 10% N_f [(A) and (B)] and 90% N_f [(C) to (G)] before failure. (**A** and **B**) SEM and HAADF-STEM images of the top surface layer of GDS SS at 10% N_f showing numerous microscale deformation bands spanning multiple dislocation cells consisting of nanosized SF segments. The inset shows a schematic diagram of the 90°and 30° Shockley partials (relative to the TEM beam direction) on FCC (111) slip planes. (**C** and **D**) SEM and bright-field TEM images at 90% N_f revealing widespread, dense, parallel microscale deformation bands intersecting multiple dislocation cells. The SAED pattern inset of these deformation bands shows parallel streaks along the [111] direction (indicated by the white arrow) due to SFs, alongside diffraction patterns of HCP martensite. (**E**) Orientation angle map revealing parallel HCP nanolayers at the topmost GDS surface measured using electron precession diffraction in TEM. (**F**) HAADF-STEM image of an individual deformation band revealing the ultrahigh density of HCP-FCC nanolaminates, along with numerous SFs. (**G**) Magnified HAADF-STEM image corresponding to the white-boxed region in (F) showing HCP nanolayers (highlighted in orange), SFs, and twin segments. In (B), (F), and (G), the dashed lines indicate (111) planes of SFs and TBs.

comparable to the spacing between opposite cell walls, whereas the average thicknesses of the HCP and FCC layers were ~5.2 nm and 7.8 nm, respectively. Therefore, a high volume fraction (~40%) of the nanolayered HCP phase formed within the microscale deformation bands. Both the SAED and HAADF-STEM results (Fig. 3, D, G, and H) indicated coherent HCP-FCC phase boundaries, with a typical orientation relationship of <0002>HCP//{111}FCC and <11$\bar{2}$0>HCP//<110>FCC. Energy-dispersive x-ray spectroscopy mapping showed uniform element distributions of all elements in both phases. These results suggest that a deformation-induced displacive transformation occurred from the austenitic FCC phase to the nanolayered martensitic HCP phase during ratcheting.

The FCC-to-HCP phase transformation, along with the formation of numerous SFs and limited TBs, introduces additional deformation mechanisms in GDS 304 SS beyond ordinary dislocation plasticity. As a result, ratcheting deformation in GDS samples involved extensive SFs and HCP activities, within fully developed dislocation cells as small as ~290 nm, leading to sustained nanoscale structural refinement. HAADF-STEM revealed numerous interlocked deformation bands in the top-layer grains, evidenced by intersecting HCP nanolayers corresponding to two HCP variants (Fig. 4, A and B). Moreover, extensive SFs formed in the FCC space between the interlocked HCP nanolayers, and these SFs frequently intersected each other or were obstructed by HCP-FCC phase boundaries (Fig. 4, B and C). By contrast, ratcheting deformation of most grains in the core of GDS samples was still dominated by extensive planar slip of full dislocations along {111} planes and loose dislocation tangles (fig. S5D). This ordinary full dislocation plasticity is similar to that observed in CG 304 SS, predominated by large dislocation cells (~500 nm) (figs. S5, A to C), as reported in most metals and alloys during ratcheting deformation (*2*, *14*, *18*, *29*).

By engineering a gradient hierarchy of dislocation cells, an unusual combination of deformation mechanisms involving SF formation and coherent FCC-to-HCP martensitic transformation can be activated, leading to significantly enhanced ratcheting resistance in GDS 304 SS along with high strength. The formation of ratcheting-regulated FCC and HCP nanolaminates is attributed to the combined effects of the following factors: the reduced characteristic length scale inherent in the GDS structure, the low SF energy of 304 SS, and the substantial cumulative plastic strain under asymmetrical cyclic stresses.

Unlike conventional plastic deformation involving full dislocation glide (*30*–*34*), the primary plastic carriers in GDS SS are Shockley partials and associated SFs. This response is mainly due to the reduced length scale of the

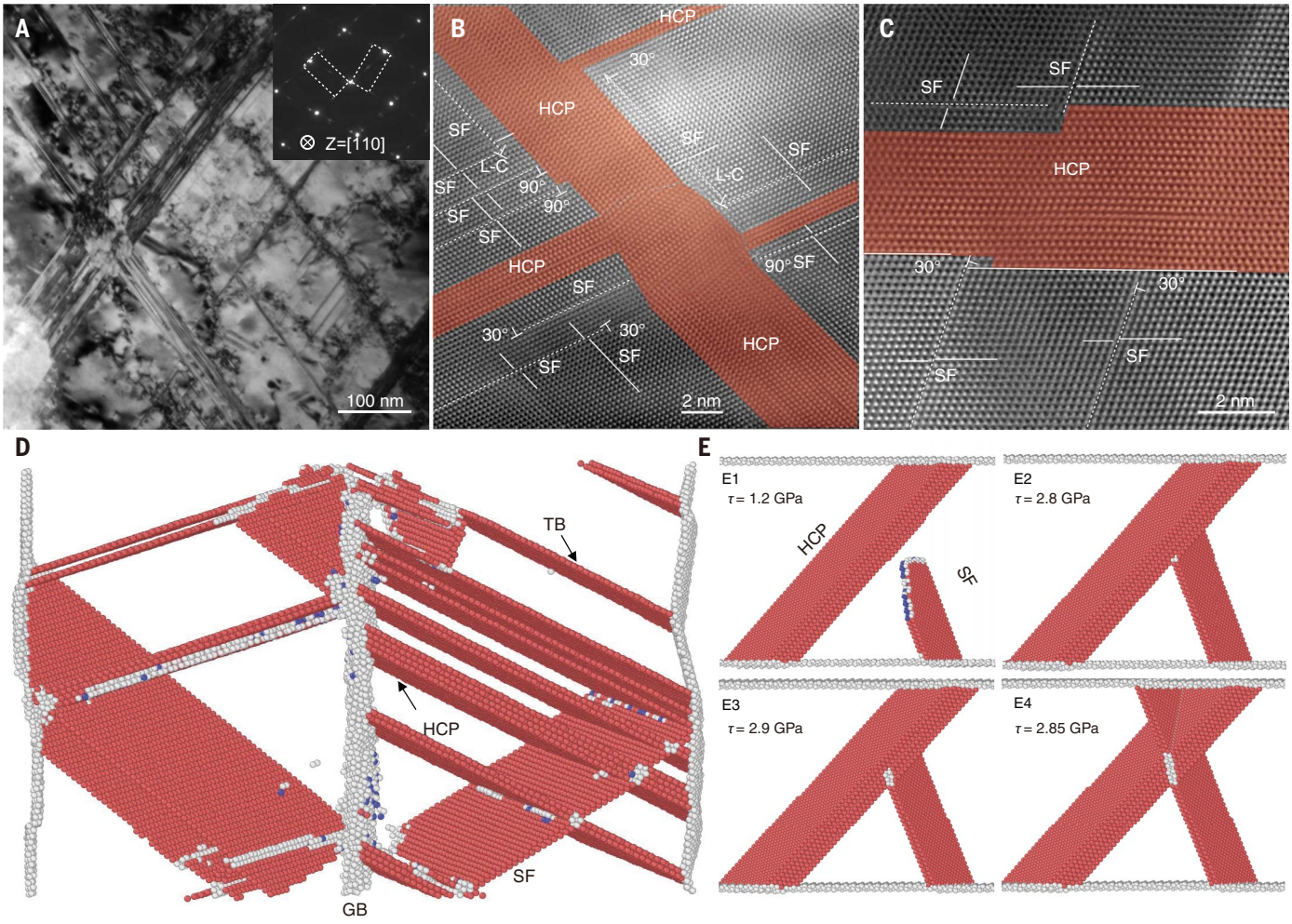

Fig. 4. Strengthening mechanisms of HCP nanolayers and SFs. (**A**) Bright-field TEM image of the topmost surface layer of GDS SS under a σ_{max} of 570 MPa at 90% N_f showing two variants of nanolayered HCP martensite intersecting each other. The inset shows SAED patterns from the intersecting HCP nanolayers. (**B**) HAADF-STEM image of a network of intersecting HCP nanolayers, SFs, and Lomer-Cottrell (L-C) locks. (**C**) Magnified HAADF-STEM image showing the interactions between an HCP nanolayer and intersecting SFs. (**D**) Atomic configurations from molecular dynamics simulation showing the formation of a network of HCP nanolayers, SFs, and TBs. Atoms in the FCC structure are omitted for clarity, and those in the HCP structure and at GBs and surfaces are colored red and white, respectively. (**E**) Atomic configurations from molecular dynamics simulation during the progressive slip transmission of an SF across an HCP nanolayer under increasing resolved shear stress τ acting on the SF (E1 to E4).

GDS structure formed through cyclic torsion. During ratcheting, significant long-range internal stresses develop to accommodate the strong structural heterogeneity introduced by the GDS structure (*26*, *35*, *36*), resulting in elevated local flow stresses, as evidenced by high microhardness values throughout GDS samples (fig. S2). To assess the effect of pretorsion on internal stresses, we estimated the internal stress level (X) of GDS samples using the yield stress difference between the prestrain and reference states: $X = \sigma_y$ (GDS) − σ_y (CG), based on tensile results (fig. S3A). By applying $(\sigma_{max} - X)/E$, the data for bulk GDS and surface GDS in Fig. 2F shift toward ratchet regime I corresponding to stage I hardening (*37*), as shown in fig. S6. According to (*37*), this stage involves low amplitudes of plastic deformation, favoring planar slip mechanisms, such as dislocation pile-up and SF formation.

High flow stresses in GDS samples provide large driving forces for the nucleation and migration of Shockley partials within highly stable dislocation cells. Additionally, the dense dislocations at cell walls serve as abundant sources for partial nucleation. Moreover, the low SF energy (~16.8 mJ/m^2) of 304 SS favors partial dislocation activity (*30*, *31*). Correspondingly, the critical size for the transition from full to partial dislocations with SFs is estimated to be ~240 nm, which closely matches the cell size (~290 nm) in the topmost GDS layer. The cumulative plastic strain of the GDS sample after a long ratcheting life of 3×10^5 cycles at a σ_{max} of 570 MPa reaches an enormous magnitude (~300), approximately three orders of magnitude greater than the net ratcheting strain (Fig. 2). The large cumulative plastic strain and associated plastic irreversibility under many cycles of asymmetrical stressing necessitate widespread SF activation. All of these factors promoting SF activity in GDS SS rarely coexist simultaneously in conventional coarse-grained or high-strength nanostructured metallic materials (*1*, *26*, *31*, *38*, *39*).

The extensive operation of partial dislocations during ratcheting deformation leads to the gradual accumulation of highly dense SFs, promoting the deformation-induced FCC-to-HCP martensitic transformation (Fig. 3 and fig. S7). The mechanism of this phase transformation differs under cyclic loading compared with monotonic loading. Under monotonic loading, the FCC-to-HCP transformation and

deformation twinning occur through the glide of Shockley partials with parallel 1/6<112> Burgers vectors of the same sense on {111} planes (*40*–*43*). By contrast, under cyclic loading, FCC-to-HCP transformation is achieved through the glide of Shockley partials with coplanar 1/6<112> Burgers vectors along different directions (Fig. 3 and fig. S7). Partial glide through alternative Burgers vectors not only effectively accommodates applied shear strains with alternating signs during cyclic stressing, but also reduces the net local plastic shear strain at the ends of each slender HCP nanolayer. Consequently, the facile partial glide reduces local deformation incompatibility between the HCP nanolayers and the FCC matrix, lowering the likelihood of damage initiation.

The nanolayered HCP martensite plays a crucial role in the strengthening and hardening responses of GDS SS during ratcheting deformation. Unlike high-angle GBs or incoherent phase boundaries (*31*, *40*), the HCP nanolayers form coherent interfaces with the FCC matrix. These coherent boundaries act as strong barriers that effectively impede the glide of dislocations and SFs on slip planes inclined to the phase boundaries (Fig. 4, A to C). Molecular dynamics simulations revealed the strong obstruction of SFs by HCP nanolayers (Fig. 4, D and E). For example, a SF on an inclined {111} slip plane in the FCC matrix was hindered by a coherent phase boundary (Fig. 4, E1 and E2). Raising the resolved shear stress barely initiated the transmission of this SF across the phase boundary (Fig. 4E3). Further increases in shear stress allowed the dislocation to glide on an inclined {10$\bar{1}$1} pyramidal plane inside the HCP nanolayer (Fig. 4, E3 and E4). Evidently, the high resistance to slip transmission stems from the strong coherent phase boundary and the high slip resistance on pyramidal planes within the HCP nanolayers (*11*, *39*).

The sustained structural refinement, from initial dislocation cells to finer networks of FCC-HCP nanolaminates and dislocation cells (Figs. 3 and 4), continuously enhanced the ability to obstruct the glide of full dislocations and partials by reducing mean free paths and segment lengths while providing abundant sources for defect nucleation and accumulation (Figs. 3 and 4). These results indicate that the increasing formation of FCC-HCP nanolaminates can sustainably enhance strain hardening and reduce dynamic recovery during asymmetrical stress cycling, thus significantly lowering ratcheting strain under prolonged cycling.

The nanolayered HCP martensite also plays a significant role in suppressing strain localization and damage accumulation in GDS SS during stress cycling, particularly compared with the mechanically induced body-centered cubic (BCC) martensite in the CG counterparts (*38*, *44*–*48*). The coherent FCC-HCP interfaces reduce local geometrical incompatibility and interfacial energy, stabilizing the HCP nanolayers by preventing heterogeneous coarsening (*11*, *39*), even at the nanoscale. These coherent interfaces, along with the aforementioned FCC-to-HCP phase transformation mediated by Shockley partials with different Burgers vector directions (Fig. 3 and fig. S7), effectively suppress fatigue damage nucleation. By contrast, uncontrolled transformation into a hard, incoherent BCC-based phase, accompanied by a large lattice dilatation (*40*), is known to be detrimental to ratcheting resistance, even for conventional TRIP steels that exhibit accelerated ratcheting and damage initiation due to phase transformation (*2*, *15*, *49*).

Three-dimensional x-ray tomography revealed the minimal cross-section contraction of GDS specimens after asymmetrical stress cycling (fig. S8, A and B), indicating their exceptional ratcheting resistance (Fig. 2). x-ray tomography further showed no discernable microcracks in GDS samples cycled to 90% N_f (fig. S8A); even after failure, cracks or dimples were only confined to regions near the fracture surface (fig. S8B). By contrast, CG samples exhibited macrocracks measuring hundreds of micrometers long on the topmost surface and numerous microcracks (tens of micrometers long) in the interior after 90% N_f (fig. S8C) resulting from widespread strain concentration and fatigue cracking. These damages were correlated with a high density of ultrafine, elongated BCC martensitic blocks (average transversal size of ~150 nm and longitudinal size ~800 nm) frequently detected near the cracks (fig. S8, D to F), similar to those found in fatigued metals with low SF energies (*1*, *29*).

The built-in gradient distribution of dislocation cells and the associated strength gradient also enhance the ratcheting resistance to GDS samples under asymmetrical stress cycling. During testing, this strength gradient leads to progressive yielding behavior and a corresponding plastic strain gradient from the soft core to the strong topmost surface (*26*, *36*). Accommodating this plastic strain gradient results in the accumulation of geometrically necessary defects, including dislocations, SFs, and martensitic HCP nanolayers (*26*, *36*). These defects contribute to sustained nonlinear kinematic and isotropic hardening for enhancing ratcheting resistance (fig. S9) (*50*). This effect is demonstrated by combining experimental measurements with a cyclic plasticity model to characterize the evolution of back stress and effective stress under asymmetric cyclic stressing. The back stress typically arises from geometrically necessary dislocations that generate long-range, directional internal stresses, whereas the effective stress originates from statistically stored dislocations that induce short-range, nondirectional internal stresses (*26*, *31*, *37*). Both impede plastic flow (*31*, *37*). Our cyclic plasticity modeling results of GDS samples (fig. S9A and table S2) closely match the measured cumulative ratcheting strain with cycles. They show a steeper hardening rate in back stress for GDS compared with CG samples under the same σ_{max}. This is evidenced by a more rapid evolution of back stress during forward and reverse loading (fig. S9, B and C) caused by enhanced hardening and reduced recovery. Consequently, the net plastic strain per cycle is smaller and thus the ratcheting rate is lower in GDS than in CG samples. This sustained nonlinear kinematic and isotropic hardening with increasing cycles in GDS samples (fig. S9, D and E) underscores the benefit of progressive microstructural refinement through the continued accumulation of SFs and FCC-HCP nanolaminates during the ratcheting deformation of GDS 304 SS.

In summary, we have achieved a combination of high strength and superior resistance to cyclic creep (ratcheting) by engineering the gradient hierarchy of dislocation cells in single-phase FCC 304 SS. Under asymmetrical cyclic stresses, continuous SF formation and FCC-to-HCP coherent martensitic transformation lead to sustained structural refinement evolving from submicrometer dislocation cells to finer networks of FCC-HCP nanolaminates within stable dislocation cells. This progressively refined microstructure enhances strain hardening, reduces dynamic recovery, and mitigates strain localization, significantly lowering cumulative ratcheting strain even after long-term cycles. The principle of sustained microstructural refinement through a gradient dislocation architecture and deformation-induced FCC-to-HCP martensitic transformations can be applied to other alloy systems by adjusting the composition or deformation conditions.

REFERENCES AND NOTES

1. S. Suresh, *Fatigue of Materials* (Cambridge Univ. Press, ed. 2, 1998).
2. G. Z. Kang, *Int. J. Fatigue* **30**, 1448–1472 (2008).
3. S. K. Paul, *J. Mater. Res. Technol.* **8**, 4894–4914 (2019).
4. H. Hübel, *Nucl. Eng. Des.* **162**, 55–65 (1996).
5. J. L. Chaboche, *Int. J. Plast.* **5**, 247–302 (1989).
6. T. Hassan, E. Corona, S. Kyriakides, *Int. J. Plast.* **8**, 117–146 (1992).
7. Y. Y. Jiang, H. Sehitoglu, *Int. J. Plast.* **10**, 849–870 (1994).
8. D. L. McDowell, *Int. J. Plast.* **11**, 397–421 (1995).
9. T. Hassan, S. Kyriakides, *Int. J. Plast.* **10**, 149–184 (1994).
10. G. Z. Kang, Y. Li, Q. Gao, Q. H. Kan, J. Zhang, *Fatigue Fract. Eng. Mater. Struct.* **29**, 93–103 (2006).
11. K. Zhang, J. R. Weertman, *Metall. Mater. Trans., A Phys. Metall. Mater. Sci.* **40**, 2255–2263 (2009).
12. C. Holste, W. Kleinert, R. Gürth, K. Mecke, *Mater. Sci. Eng. A* **187**, 113–123 (1994).
13. F. Lorenzo, C. Laird, *Acta Metall.* **32**, 681–692 (1984).
14. K. Dutta, S. Sivaprasad, S. Tarafder, K. K. Ray, *Mater. Sci. Eng. A* **527**, 7571–7579 (2010).
15. S. Chang, Z. Zhu, X. Huang, J. Zhang, G. Kang, *Int. J. Fatigue* **181**, 108118 (2024).
16. X. C. Lu *et al.*, *J. Mech. Phys. Solids* **142**, 103971 (2020).
17. G. Z. Kang, Q. Gao, L. Cai, X. Yang, Y. Sun, *J. Mater. Sci. Technol.* **17**, 219–223 (2001).
18. P. Lukáš, L. Kunz, *Mater. Sci. Eng. A* **322**, 217–227 (2002).
19. S. Cheng *et al.*, *Acta Mater.* **57**, 1272–1280 (2009).
20. M. Zhang *et al.*, *Int. J. Fatigue* **121**, 252–264 (2019).
21. Y. Wu, J. Yang, X. Shen, R. Zhu, *J. Mater. Eng. Perform.* **26**, 837–842 (2017).

22. C. Backes, M. Smaga, T. Beck, *Int. J. Fatigue* **186**, 108410 (2024).
23. Q. Pan *et al*., *Science* **374**, 984–989 (2021).
24. Q. Pan *et al*., *Science* **382**, 185–190 (2023).
25. K. H. Lo, C. H. Shek, J. K. L. Lai, *Mater. Sci. Eng. Rep.* **65**, 39–104 (2009).
26. X. Y. Li, L. Lu, J. Li, X. Zhang, H. Gao, *Nat. Rev. Mater.* **5**, 706–723 (2020).
27. Y. M. Wang *et al*., *Nat. Mater.* **17**, 63–71 (2018).
28. S. Sinha, S. Ghosh, *Int. J. Fatigue* **28**, 1690–1704 (2006).
29. P. Peralta, C. Laird, in *Physical Metallurgy*, D. E. Laughlin, K. Hono, Eds. (Elsevier, ed. 5, 2014), pp. 1765–1880.
30. J. P. Hirth, J. Lothe, *Theory of Dislocations* (Cambridge Univ. Press, 2017).
31. A. S. Argon, *Strengthening Mechanisms in Crystal Plasticity* (Oxford Univ. Press, 2008).
32. J. C. Stinville *et al*., *Science* **377**, 1065–1071 (2022).
33. S. Lavenstein, Y. Gu, D. Madisetti, J. A. El-Awady, *Science* **370**, eabb2690 (2020).
34. Q. Pan, H. Zhou, Q. Lu, H. Gao, L. Lu, *Nature* **551**, 214–217 (2017).
35. H. Mughrabi, *Acta Metall.* **31**, 1367–1379 (1983).
36. Y. T. Zhu *et al*., *Mater. Res. Lett.* **9**, 1–31 (2020).
37. X. Feaugas, C. Gaudin, *Int. J. Plast.* **20**, 643–662 (2004).
38. X. S. Yang, S. Sun, T.-Y. Zhang, *Acta Mater.* **95**, 264–273 (2015).
39. A. Pineau, A. Amine Benzerga, T. Pardoen, *Acta Mater.* **107**, 508–544 (2016).
40. J. W. Christian, *The Theory of Transformations in Metals and Alloys* (Elsevier, ed. 3, 2002).
41. H. He *et al*., *Nano Lett.* **21**, 1419–1426 (2021).
42. H. Fujita, S. Ueda, *Acta Metall.* **20**, 759–767 (1972).
43. G. B. Olson, M. Cohen, *Metall. Trans., A* **7**, 1897–1904 (1976).
44. G. B. Olson, M. Cohen, *J. Less Common Met.* **28**, 107–118 (1972).
45. T. Suzuki, H. Kojima, K. Suzuki, T. Hashimoto, M. Ichihara, *Acta Metall.* **25**, 1151–1162 (1977).
46. K. P. Staudhammer, L. E. Murr, S. S. Hecker, *Acta Metall.* **31**, 267–274 (1983).
47. J. A. Venables, *Philos. Mag.* **7**, 35–44 (1962).
48. Y. Li *et al*., *Science* **379**, 168–173 (2023).
49. M. Soleimani, A. Kalhor, H. Mirzadeh, *Mater. Sci. Eng. A* **795**, 140023 (2020).
50. N. Ohno, J. D. Wang, *Int. J. Plast.* **9**, 375–390 (1993).

ACKNOWLEDGMENTS

We thank J. P. Cui for performing HAADF-STEM experiments; S. G. Wang, C. J. Li, and L. Zhang for performing x-ray experiments and analyzing the results; and C. H. Li for performing the EBSD experiments. **Funding:** Q.P. and L.L. acknowledge financial support from the National Science Foundation of China (NSFC, grants 92463302, 92163202, 52122104, 52471151, and 52071321) and from the international partnership program of the Chinese Academy of Sciences (CAS grant 172GJHZ2023075GC). Q.P. is supported by the Excellent Youth Innovation Promotion Association and Strategic Priority Research Program, CAS. N.L. is supported by the Shandong Excellent Young Scientists Fund Program (Overseas) (grant 2023HWYQ-041). **Author contributions:** L.L. and T.Z. initiated and supervised the project. Q.P. and S.G. prepared the sample and performed the experiments. Q.P. and N.L. guided and analyzed TEM results. K.D. and T.Z. performed atomistic and cyclic plasticity simulations. Q.P., L.L., and T.Z. designed the experiments and drafted the manuscript. All coauthors contributed to the discussions and revised the manuscript. **Competing interests:** The authors declare no competing interests. **Data and materials availability:** All data are available in the main manuscript or the supplementary materials.

SUPPLEMENTARY MATERIALS

science.org/doi/10.1126/science.adt6666
Materials and Methods
Supplementary Text
Figs. S1 to S9
Tables S1 and S2
References (*51*–*66*)

Submitted 7 October 2024; accepted 20 February 2025
10.1126/science.adt6666